Catalysis Science & Technology

ROYAL SOCIETY OF CHEMISTRY

PAPER

View Article Online
View Journal | View Issue

Cite this: *Catal. Sci. Technol.*, 2023, **13**, 6068

Cu nanoparticles confined in siliceous MFI zeolite for methanol steam reforming†

Yang Hong,[ab] Yijun Zheng,[a] Nana Yan,[ab] Xiaona Liu,[ab] Peng Guo *[ab] and Zhongmin Liu[ab]

Received 20th August 2023,
Accepted 13th September 2023

DOI: 10.1039/d3cy01165h

rsc.li/catalysis

The methanol steam reforming (MSR) reaction is a sustainable process for producing hydrogen using solar energy. However, Cu-based catalysts often suffer from sintering issues. In this study, we prepared Cu nanoparticles confined in the siliceous MFI-type silicate-1 using a ligand-stabilized strategy, referred to as Cu@S-1. Compared with the Cu/S-1 catalyst prepared through conventional impregnation, the Cu@S-1 catalyst displayed highly active and stable performance in the MSR reaction. The 1.0 Cu@S-1 catalyst achieved a methanol conversion of 72% and a CO selectivity of 0.2% at 300 °C. Comprehensive characterization studies revealed that the 1.0 Cu@S-1 catalyst exhibited an enhanced dispersion of Cu species and a higher Cu^+ ratio due to the enhanced interaction between Cu species and the zeolite framework.

1. Introduction

With fossil fuel combustion and environmental degradation, investigations regarding hydrogen have drawn increasing attention. Hydrogen is a good renewable energy carrier with the highest energy density and no pollution.[1–5] However, gaseous hydrogen storage and transport are still challenging. Liquid sunshine methanol utilized as a liquid hydrogen carrier would be a suitable choice. Compared with gaseous hydrogen, methanol displays unique advantages, such as easy storage and transport, the highest C/H ratio among organics, low sulphur content, and low reforming temperature.[6] Hydrogen can be extracted from methanol *via* four alternatives, methanol decomposition (MD),[7] the partial oxidation of methanol (POM),[8] methanol steam reforming reaction (MSR),[9] and oxidative steam reforming of methanol (OSRM).[10] Among these techniques, the MSR reaction possesses various advantages, such as low reaction temperature, low carbon monoxide selectivity, and high hydrogen yield. Although the reverse water gas shift reaction, eqn (2), and the methanol decomposition reaction, eqn (3), may also exist in the MSR reaction, eqn (1) is still considered an efficient approach to generate hydrogen.[11,12]

$$CH_3OH + H_2O \rightleftharpoons CO_2 + 3H_2 \quad (1)$$

$$CO_2 + H_2 \rightleftharpoons CO + H_2O \quad (2)$$

$$CH_3OH \rightleftharpoons CO + 2H_2 \quad (3)$$

Catalysts for the MSR reaction can be categorized into two groups. One is a group VIII–X noble metal catalyst, while the other is a Cu-based catalyst. For VIII–X noble metals, palladium and platinum loaded on various supports (such as ZnO, Al_2O_3, SiO_2, and carbon) have been extensively investigated, for example, Pd/ZnO and Pt/ZnO exhibit high activity at low temperatures (about 220 °C).[13–17] However, their CO selectivity is generally greater than 30%, which leads to the expensive postprocessing for purifying H_2. Such high selectivity of CO may arise from the direct decomposition of methanol. To further decrease the concentration of CO in the reforming gas, Peter Wasserscheid *et al.* studied the influence of alkali metal salt in the MSR reaction over the Pt/Al_2O_3 and found that both activity and selectivity are enhanced by Li/K/Cs acetate salt coating.[18] Very recently, Ding Ma *et al.* creatively modified Pt and/or Ni with α-MoC, which shows excellent performance in MSR with high activity and low CO selectivity at low temperatures.[9,19]

Compared with noble metal catalysts, Cu-based catalysts exhibit obvious advantages, including low cost, high catalytic activity, and excellent selectivity to CO_2 and H_2 at relatively mild temperatures (200–300 °C).[20–25] However, the poor thermal stability leads to the Cu particles sintering easily and catalyst deactivation. The predominant sintering mechanism in bulk metals relates to cohesive energy. Hughes put forward

[a] *National Engineering Research Center of Lower-Carbon Catalysis Technology, State Energy Low Carbon Catalysis and Engineering R&D Center, Dalian National Laboratory for Clean Energy, Dalian Institute of Chemical Physics, Chinese Academy of Sciences, Dalian, China. E-mail: pguo@dicp.ac.cn*
[b] *University of Chinese Academy of Sciences, Beijing, China*

† Electronic supplementary information (ESI) available. See DOI: https://doi.org/10.1039/d3cy01165h

the following order of stability for metals: Ag < Cu < Au < Pd < Fe < Ni < Co < Pt < Rh < Ru < Ir < Os < Re.[26] There is no doubt that Cu-based catalysts suffer from serious sintering. Searching for better supports to stabilize Cu species is still a great challenge for the MSR reaction. For Cu-based catalysts, the activity and selectivity are closely related to the metal size and their specific surface area. To attain the narrow metal size distribution and the high specific surface area, various additional metal oxides are also introduced to the supports. For example, the addition of ZnO to Cu/Al_2O_3 enhances the Cu dispersion, while the introduction of ZrO_2 improves the CO selectivity.[25,27]

Besides the aforementioned nanoparticles (including noble metal and Cu) stabilized by various oxides, zeolites that possess ordered channels/cavities, large surface area and fantastic thermal stability are ideal supports that can be utilized to confine or load such nanoparticles. In this case, nanoparticles embedded in the zeolite matrix will result in the alleviation of sintering. The most popular and convenient strategy is the ligand-stabilized approach to encapsulate ultra-small noble and their alloys within siliceous zeolites by one-pot synthesis.[28–34] For instance, Corma and co-workers successfully encapsulated sub-nanometer PtSn clusters within siliceous **MFI**-type zeolites, which exhibit excellent properties in the propane dehydrogenation (PDH) reaction.[28] The propylene selectivity was maintained at 98% and the lifetime was more than 30 hours. Yu's group employed diethylamine as the ligand-stabilizer, encapsulating Pd and $Ni(OH)_2$ in silicate-1, which displayed an ultrahigh activity in the formic acid decomposition with no CO detected.[29] Comparing with the commercial Pd/C, $PdNi(OH)_2$@S-1 displayed a 3-fold higher activity, and the TOF could reach 5800 h^{-1} at 60 °C. Xiao *et al.* synthesized Pt@S-1 by employing PVP to stabilize the Pt nanoparticles, which displayed an ultrahigh activity in the CO redox reaction.[30] Comparing with the impregnation method, the temperature for total conversion of CO was much lower over Pt@S-1. Pt@S-1 displayed higher stability in the cyclic experiment. Recently, Ding *et al.* employed a multi-step synthesis strategy to develop the Cu@Na-beta catalyst, which exhibited remarkable performance in the hydrogenation of CO_2 to ethanol. The catalyst achieved a high CO_2 conversion rate of 7.5% and demonstrated nearly 100% selectivity towards ethanol among the organic products.[35] To the best of our knowledge, the one-pot encapsulation of inexpensive nanoparticles in the siliceous zeolites through the ligand-stabilized approach dedicated for the potential industrial applications is still rare.[31,36]

Herein, we utilize the ligand-stabilized approach for confining Cu species into siliceous **MFI**-type zeolite silicate-1, which was subsequently reduced by H_2 (denoted as Cu@S-1). Compared with the impregnation method (denoted as Cu/S-1), this method is facile and results in the high dispersion of Cu species within the silicate-1 zeolite matrix. After optimizing parameters, such as Cu content and reaction temperatures, a robust catalyst with 1% Cu (designated as 1.0 Cu@S-1) was identified. Compared with 1.0 Cu/S-1, 1.0 Cu@S-1 showed better MSR activity and stability. XRD, SEM, TEM, H_2-TPR, *operando* XPS, and *in situ* CO-FTIR techniques were employed to investigate the physical and chemical properties.

2. Experimental

2.1 Catalyst preparation

A solution of Cu(II)–tetraethylenepentamine (TEPA) was prepared by mixing 1.0 g of $CuSO_4$ in 20 mL aqueous solution with 1.2 g TEPA (90%) under continuous stirring at room temperature until complete dissolution.

For example, in a typical synthesis of 1.0 Cu@S-1, 29.05 g of TPAOH (25%) was mixed with 76.28 g deionized water for 10 minutes under stirring, and then 18.18 g TEOS was added to the mixture. The obtained mixture was further stirred for 6 hours to achieve the hydrolysis of TEOS. Next, 2.660 g Cu(II)–TEPA was introduced by drop-wise addition and then stirred for 30 minutes. The gel was transferred into a Teflon autoclave and maintained at 180 °C for 24 hours. The samples were washed three times with deionized water and dried at 100 °C overnight. Then, the as-synthesized samples were calcinated at 600 °C for 4 hours to remove the templates.

The 1.0 Cu/S-1 catalyst was obtained using the wet impregnation method. $Cu(NO_3)_2{\cdot}3H_2O$ (0.038 g) was dissolved in deionized water, and the calcined silicate-1 zeolite (1.0 g) was added to the copper nitrate solution. After stirring at 80 °C until dry, followed by drying at 100 °C overnight to remove water, and after calcining at 600 °C for 4 hours, the 1.0 Cu/S-1 catalyst was obtained.

The $CuZnO/SiO_2$ catalyst was prepared by the wet impregnation method. $Cu(NO_3)_3{\cdot}3H_2O$ (0.038 g) and $Zn(NO_3)_2{\cdot}6H_2O$ (0.046 g) were dissolved in deionized water, and SiO_2 (1.0 g) was added to the solution. After stirring at 80 °C until dry, followed by drying at 100 °C overnight, to remove water, and finally calcined at 600 °C for 4 hours, the $CuZnO/SiO_2$ catalyst was obtained.

2.2 Catalyst characterization

The crystallinity and morphology of the catalysts were studied using XRD, SEM, and HRTEM. A PANalytical X'Pert PRO X-ray diffractometer with Cu-Kα radiation (λ = 0.15418 nm) was employed to collect the XRD data, operating at 40 kV and 40 mA. The loading amount of Cu was measured using a PhilipsMagix-601 X-ray fluorescence (XRF) spectrometer. The Cu loading of 1.0 Cu@S-1 was further detected by coupled plasma optical emission spectroscopy (ICP-OES) on an ICP-OES 7300DV instrument (PerkinElmer) with a sensitivity line of 349.8 nm and a detection range of 1–10 ppm. The surface area and pore volume of the catalyst were calculated using N_2 adsorption–desorption isotherms using a Micromeritics ASAP2020 instrument at −196 °C. The BET equation and *t*-plot methods were employed to evaluate the total surface area and pore volume, respectively.

The reduction behaviour of the catalysts was analysed with H_2-temperature programmed reduction (TPR) using a chemisorption analyser Micromeritics AutoChem II 2920 equipped with a thermal conductivity detector (TCD). For H_2-TPR, samples were heated under 10% volume H_2/Ar, and the temperature was programmed from 50 °C to 800 °C at a ramping rate of 10 °C min^{-1}. The dispersion of Cu species in the catalysts was determined by N_2O chemisorption. The catalysts were heated under 10% volume H_2/Ar, and the temperature was programmed to rise from 50 °C to 400 °C at a ramping rate of 10 °C min^{-1}, the amount of hydrogen consumption in the first TPR was denoted as A_1. Then, the reactor was purged with Ar at 50 °C. A flow of 10% N_2O/Ar (30 mL min^{-1}) was used to oxidize the surface Cu atoms to Cu_2O at 50 °C for 30 minutes. The reactor was flushed with Ar to remove the oxidant. Finally, another TPR experiment was performed in 10% H_2/Ar at a flow rate of 30 mL min^{-1} until 400 °C. Hydrogen consumption in the second TPR was denoted as A_2. The dispersion (D_{Cu}) is calculated according to the following equation:[37]

$$D_{Cu} = \frac{2A_2}{A_1} \times 100\%$$

Thermogravimetric analysis (TGA) was performed to evaluate the coke content of the unloaded catalysts. 150 mg of the catalyst was heated to 800 °C under an air atmosphere at a ramping rate of 10 °C min^{-1}, and the weight loss of 330 to 650 °C was used to calculate the coke content.

The high-angle annular dark-field scanning transmission electron microscopy (HAADF-STEM) and energy dispersive X-ray spectra (EDX-mapping) images displayed in Fig. 1c, 2 and 5, respectively, were obtained using a JEOL JEM-ARM200F instrument. The iDPC-STEM image shown in Fig. 1d was obtained using the Thermo Scientific Themis G3 ETEM. The HAADF-STEM images displayed in Fig. S2, S8, and S9† were collected using a JEOL JEM-F200 instrument.

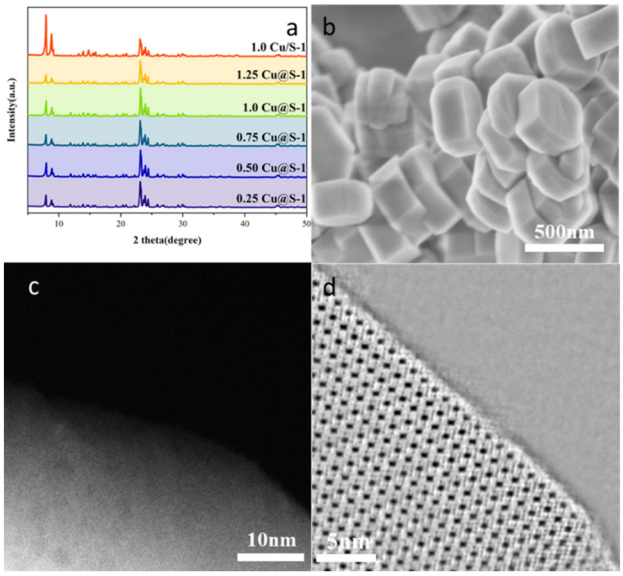

Fig. 1 (a) PXRD patterns of *x* Cu@S-1 and 1.0 Cu/S-1. (b) SEM image of 1.0 Cu@S-1. (c) HAADF-STEM and (d) iDPC-STEM image of the calcined 1.0 Cu@S-1.

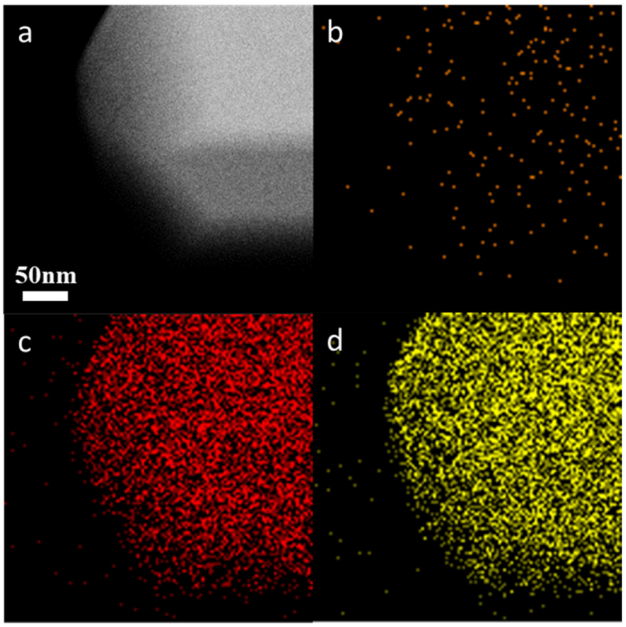

Fig. 2 (a) HAADF-STEM image of 1.0 Cu@S-1 and corresponding EDX mapping of (b) Cu, (c) O, and (d) Si.

The *operando* X-ray photoelectron spectroscopy (XPS) analysis was conducted on an ESCALAB 250Xi spectrometer using an Al Kα (*hv* = 1486.6 eV) X-ray source with a pass energy of 100 eV, and the base pressure of the analysis chamber less than 1×10^{-8} Pa. To obtain the spectra of the freshly reduced catalyst, the calcined samples were treated at 573 K in hydrogen for 2 h and then cooled to room temperature without exposure to air for the XPS measurements.

In situ CO Fourier transform infrared spectroscopy (FTIR) analysis was measured using a BRUKER TENSOR27 spectrometer. Each spectrum consisted of 32 scans and was collected with a resolution of 4 cm^{-1}. To obtain the spectra of the reduced catalysts, the calcined samples were reduced in hydrogen at 573 K for 2 hours and then cooled to room temperature. Then, CO was introduced to the chamber until the saturation, and then N_2 was introduced into the chamber to sweep the unabsorbed CO.

2.3 Catalytic test

Methanol steam reforming was carried out in a fixed-bed reactor with a 10 mm inner diameter. A catalyst loading of 0.5 g was placed in the reactor and positioned in the middle of the temperature-controlled zone of the furnace. Prior to the reaction, the catalyst was reduced at 300 °C for 2 hours using pure H_2 flow (34 mL min). A flow of methanol and H_2O (44 wt% methanol) in a constant ratio was heated to the

setting temperature, and subsequently introduced into the fix-bed reactor with nitrogen (34 mL min). Product analysis was performed using online gas chromatography (GC) equipped with a flame ionization detector (FID) and a thermal conductivity detector (TCD).

CH_3OH conversion was calculated using the following equation:

$$CH_3OH\ \text{conversion} = \frac{CH_3OH_{in} - CH_3OH_{out}}{CH_3OH_{in}}$$

Product selectivities were calculated using the following equations:

$$S(H_2) = \frac{f_{H_2}A_{H_2}}{f_{H_2}A_{H_2} + f_{CO_2}A_{CO_2} + f_{CO}A_{CO}}$$

$$S(CO_2) = \frac{f_{CO_2}A_{CO_2}}{f_{H_2}A_{H_2} + f_{CO_2}A_{CO_2} + f_{CO}A_{CO}}$$

$$S(CO) = \frac{f_{CO}A_{CO}}{f_{H_2}A_{H_2} + f_{CO_2}A_{CO_2} + f_{CO}A_{CO}}$$

3. Results and discussion

3.1 Structural characterizations of Cu@S-1

A series of x Cu@S-1catalysts (x denoted as weight percent of Cu) were synthesized from a gel with a chemical composition of 1 TEOS : 0.5 TPAOH : 70 H_2O : x Cu–TEPA (x = 0.0023–0.0117) at 180 °C for 24 hours. From the XRD patterns, as shown in Fig. 1a, all catalysts presented the typical **MFI**-type structure. Diffraction peaks for crystalline Cu were not observed. The texture properties and Cu contents of the as-calcined catalysts are shown in Table S1.† The N_2 adsorption and desorption isotherms of 1.0 Cu@S-1, as shown in Fig. S1,† show a typical type I isotherm, and it displayed that micropore volumes are dominant in such catalysts. Fig. S1† shows that 1.0 Cu@S-1 has an external surface area of 356 $m^2\ g^{-1}$ and a micropore volume of 0.13 $cm^3\ g^{-1}$. The XRF results shown in Table S1† indicate the Cu loading amounts as 0.26%, 0.53%, 0.73%, 1.05%, and 1.21%, respectively. The ICP-OES result of 1.0 Cu@S-1 agreed with the XRF results.

The SEM image shows the 1.0 Cu@S-1 catalyst with a thickness of about 200 nm and a typical coffin morphology, as seen in Fig. 1b. The size of the Cu nanoparticles in the calcined 1.0 Cu@S-1 catalyst was probed using HAADF-STEM, as presented in Fig. 1c. This indicates that there were no apparent Cu nanoparticles in the calcined 1.0 Cu@S-1. The emerging advanced imaging technique called iDPC-STEM was applied to the calcined 1.0 Cu@S-1 catalyst, as shown in Fig. 1d. It showed that the projection of silicate-1 along the [010] direction can be clearly observed, including 10-ring pore openings, and the Cu nanoparticles were absent, as shown in Fig. 1d. The HAADF-STEM images revealed that in the synthesized 1.0 Cu@S-1, the Cu species were highly dispersed in the zeolite's matrix during the hydrothermal synthesis. However, for the calcined 1.0 Cu/S-1, there were obvious Cu nanoparticles, as shown in Fig. S2.† The size of the Cu nanoparticles is about 3 nm, and they tend to aggregate with each other. Moreover, the EDX mapping results of the calcined 1.0 Cu@S-1 (Fig. 2a–d) also confirmed the uniform distribution and complete encapsulation of Cu species in silicate-1.

H_2-TPR experiments on calcined 1.0 Cu@S-1 and 1.0 Cu/S-1 were conducted to study the reduction temperature, as shown in Fig. S3.† Over 1.0 Cu/S-1, the peak appeared at 240 °C, which can be ascribed to the reduction of CuO_x to metallic Cu, while the main peak of the 1.0 Cu@S-1 lied at about 300 °C. These results indicate that Cu species in 1.0 Cu@S-1 were firmly surrounded by the zeolite framework, resulting in a higher reduction temperature compared with 1.0 Cu/S-1. Previous studies have reported that the reduction temperature of the encapsulated Cu in the zeolite is higher than that for CuO impregnated on zeolite.[35,38] Furthermore, the N_2O chemisorption results demonstrate that the dispersion of Cu species in 1.0 Cu@S-1 is much higher than that in 1.0 Cu/S-1 (Table S1†). The disparity in Cu species dispersion will subsequently impact the stability and activity of both catalysts.

3.2 Catalytic performance of 1.0 Cu@S-1

Fig. 3a illustrates the MSR catalytic performance of a series of reduced x Cu@S-1 catalysts at 300 °C. As the Cu loading amount increases from 0.25 wt% to 1.0 wt%, the methanol conversion increases from 15% to 70%. However, with a further increase in Cu loading to 1.25 wt%, the conversion decreases to 50%. The N_2O chemisorption results (Table S1†) indicate that the dispersion of Cu species in 1.0 Cu@S-1 is higher than that in 1.25 Cu@S-1. The disparities in the dispersion between the two catalysts impact their catalytic activities. Among the various x Cu@S-1 catalysts, the 1.0 Cu@S-1 catalyst exhibits promising MSR performance with high methanol conversion and low CO selectivity.

We further investigated the effect of temperature on this reaction using the 1.0 Cu@S-1 catalyst, as shown in Fig. 3b. The results demonstrate that as the temperature increases from 280 °C to 340 °C, the methanol conversion increases from 60% to 90%, and the CO selectivity increases from 0.09% to 1.9%. The increase in CO selectivity may be attributed to methanol decomposition or the reverse water-gas shift reaction as the temperature increases. Therefore, through comprehensive investigations regarding methanol conversion, CO selectivity, and reaction temperature, the optimized catalyst 1.0 Cu@S-1 is still the promising catalyst for the MSR reaction among these catalysts. However, the methanol conversion over 1.0 Cu/S-1 slowly increases up to 50% and then the activity sharply declines as displayed in Fig. S4.† The methanol conversion over 1.0 Cu@S-1 catalyst increases in the first 4 hours and is maintained stable over 20 h. After the 20 h reaction, the methanol conversion over

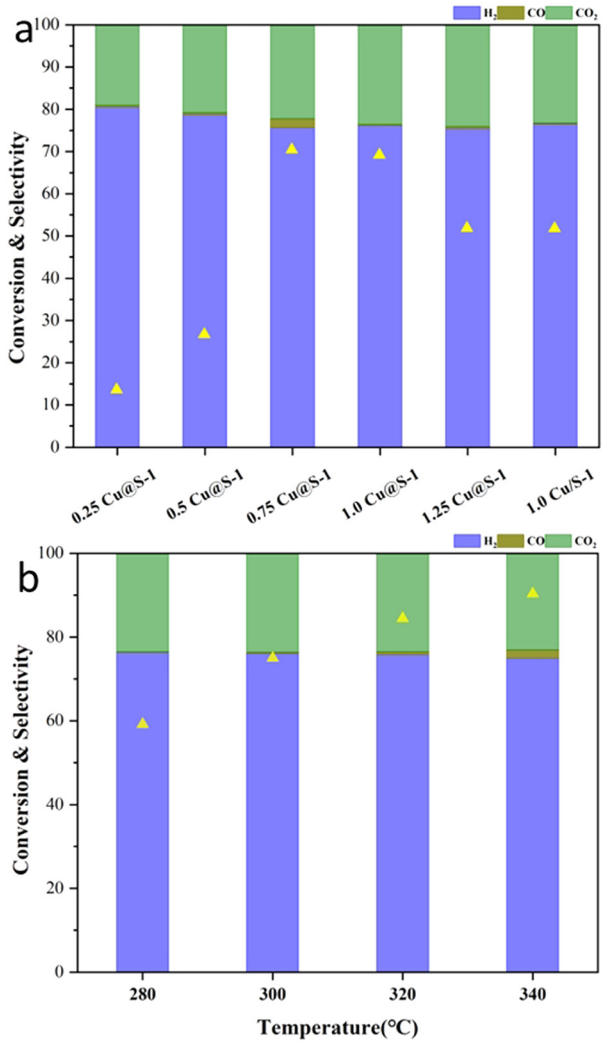

Fig. 3 (a) Methanol conversion and H_2/CO/CO_2 selectivity over different catalysts at 300 °C. (b) Methanol conversion *versus* 280 to 340 °C over 1.0 Cu@S-1. Reaction conditions: 44% methanol, N_2 at a rate of 34 mL min^{-1}, WHSV = 4.55 h^{-1}, 1 atm.

the 1.0 Cu@S-1 is still about 72%, which is double the 1.0 Cu/S-1. Interestingly, the catalytic performance of 1.0 Cu@S-1 in the MSR process surpasses that of the CuZnO/SiO_2 catalyst with a comparable Cu loading of 1.18% and a Zn loading of 1.18% (Fig. S4†). In the stability test, the 1.0 Cu@S-1 catalyst showed significant stability with about 34% methanol conversion and 0.1% CO selectivity after 40 hours on time-on-stream (TOS) at different temperatures, as depicted in Fig. S5.† Moreover, compared to Cu nanoparticles prepared using the impregnation method, the Cu nanoparticles confined within the zeolite framework through the ligand-stabilized strategy exhibit higher stability.

3.3 Comparative analysis of 1.0 Cu@S-1 and 1.0 Cu/S-1 catalysts

In situ FTIR measurements were employed to detect the electronic states of the Cu sites in the reduced catalyst (Fig. S6†) using CO as the probe molecule. The reduced 1.0 Cu@S-1 and 1.0 Cu/S-1 exhibit the obvious bands at 2127 cm^{-1} and 2124 cm^{-1}, which can be ascribed to the linear-bonded Cu^+–CO species.[39,40] Moreover, the *operando* XPS was employed to further investigate existing states of Cu, which are crucially important for the MSR reaction. As shown in Fig. 4a, the Cu $2p_{3/2}$ and $2p_{1/2}$ peak banding energies of the calcined 1.0 Cu/S-1 are 934.0 and 953.7 eV, respectively, which are consistent with the banding energy of the Cu^{2+}.[41,42] Furthermore, there are accompanying shakeup satellites (940–945 eV) in the calcined 1.0 Cu/S-1, which indicate that Cu species are present as CuO. Moreover, the Cu LMM spectrum reveals that there are both Cu^{2+} and Cu^+ in the calcined 1.0 Cu/S-1. After the reduction, the Cu $2p_{3/2}$ shifts to 933.3 eV, and there are two peaks at 917.6 and 913.9 eV in the Cu LMM spectrum, which can be ascribed to Cu^0 and Cu^+, respectively. Meanwhile, for the calcined 1.0 Cu@S-1, the Cu $2p_{3/2}$ has a banding energy is 935.0 eV and the Cu LMM spectrum displays two peaks at 913.5 and 916.5 eV (as illustrated in Fig. 4b), which can be ascribed to Cu^+ and Cu^{2+}, respectively. After reduction at 300 °C for 2 hours, the Cu $2p_{3/2}$ of 1.0 Cu@S-1 shifts to 932.8 eV. Cu^+ and Cu^0 are further recognised from the Cu LMM spectra. From the deconvolution of the Cu LMM spectra, two peaks at 917.6 and 913.9 eV were observed, which indicated the coexistence of Cu^+ and Cu^0 in the reduced 1.0 Cu@S-1. Based on the XPS results, both Cu^{2+} and Cu^+ were found in both calcined catalysts. Furthermore, the XPS spectra indicated that the reduced 1.0 Cu@S-1 catalyst had a Cu^+/Cu^0 ratio of 2.6, whereas the reduced 1.0 Cu/S-1 catalyst had a ratio of 1.5. This increase in the Cu^+ ratio is expected to enhance methanol conversion, which is consistent with previous findings. For example, Li *et al.* reported similar results, establishing a linear correlation between the turnover of frequency (TOF) and the ratio of $Cu^+/(Cu^+ + Cu^0)$.[43]

Finally, we investigated the coke deposition behaviour of the spent 1.0 Cu@S-1 and 1.0 Cu/S-1 catalysts. The thermogravimetric analysis (TGA) curves, depicted in Fig. S7,† demonstrate that both catalysts exhibited negligible coke depositions. The TGA results indicate that the zeolite support could inhibit the coke generation. Spent 1.0 Cu@S-1 and 1.0 Cu/S-1 catalysts were also investigated by HAADF-STEM imaging, as shown in Fig. S8 and S9,† respectively. Apparent Cu nanoparticles are observed in the 1.0 Cu@S-1 sample, with a particle size of approximately 2–4 nm. In contrast, the Cu nanoparticles on the 1.0 Cu/S-1 catalyst exhibit an increased size of 5 nm. EDX images of the spent 1.0 Cu@S-1, as depicted in Fig. 5, indicate that Cu aggregation occurred in contrast to the calcined 1.0 Cu@S-1 (Fig. 2a). HAADF-STEM images of the spent samples reveal that the Cu species confined within the zeolite's framework are able to prevent sintering under a redox atmosphere at relatively high temperatures. Differences in the size and dispersion of the Cu species in both samples lead to different methanol conversions after a TOS of 20 hours.

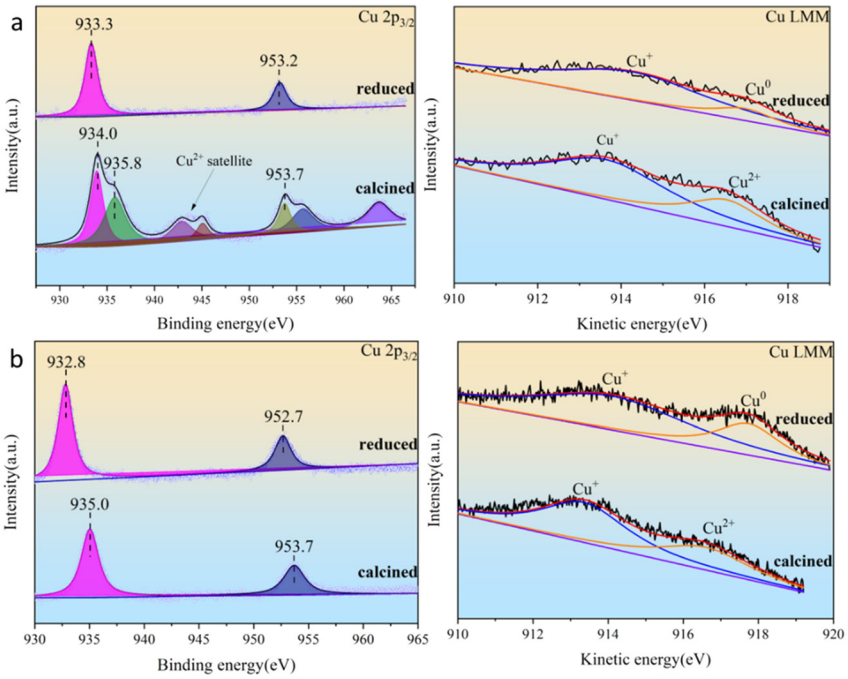

Fig. 4 *Operando* Cu 2p XPS spectra of calcined and reduced (a) 1.0 Cu/S-1 and (b) 1.0 Cu@S-1 and corresponding Cu LMM spectra.

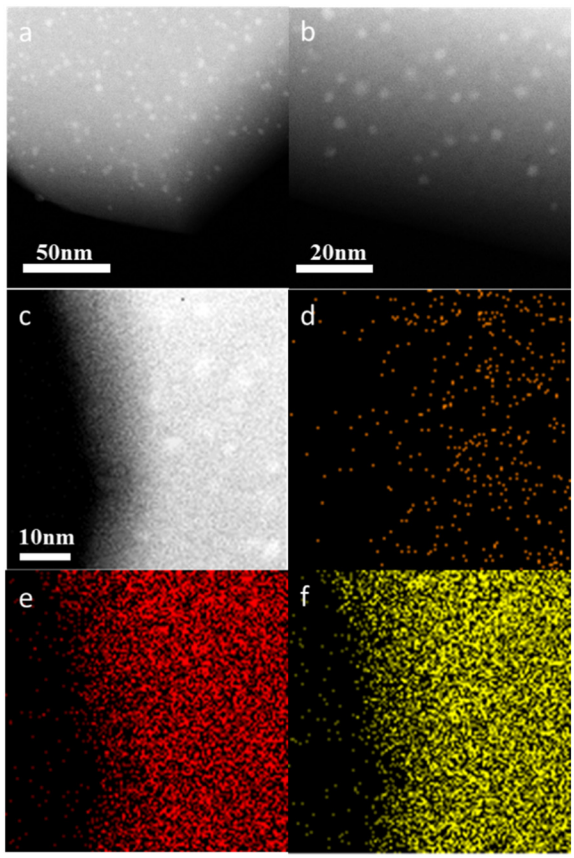

Fig. 5 (a–c) HAADF-STEM images of the spent 1.0 Cu@S-1 and corresponding EDX mapping of (d) Cu, (e) O, and (f) Si.

Compared with the 1.0 Cu/S-1 catalyst, the 1.0 Cu@S-1 catalyst with Cu nanoparticles confined in the zeolite framework demonstrates higher methanol conversion and sustained stability in the MSR reaction. The ligand-stabilized strategy for confining Cu nanoparticles in silicate-1 efficiently inhibits their agglomeration, as evidenced by the HAADF-STEM images. The analysis of XPS, FTIR, and N_2O chemisorption results confirms a higher abundance of Cu^+ species in the reduced 1.0 Cu@S-1 catalyst, accompanied by a greater dispersion compared to the 1.0 Cu/S-1 catalyst. Overall, the enhanced dispersion of Cu species, increased Cu^+ ratio, and the stabilizing influence of the zeolite matrix collectively improve the activity and stability of the 1.0 Cu@S-1 catalyst in the MSR reaction.

4. Conclusion

In summary, we synthesized a robust catalyst, 1.0 Cu@S-1, for the MSR reaction, which effectively suppresses Cu nanoparticle sintering and reduces coke deposition. This catalyst demonstrates high activity and stability with low CO selectivity and no CH_4 by-product. *Operando* XPS, *in situ* CO-FTIR spectra, and N_2O chemisorption revealed a higher abundance of Cu^+ species in 1.0 Cu@S-1, contributing to its enhanced activity. The zeolite matrix plays a dual role by confining Cu nanoparticles and stabilizing Cu^+ species, resulting in long-term stability. This study provides valuable insights for the design of non-noble metal catalysts with improved stability and selectivity in the MSR reaction.

Conflicts of interest

There are no conflicts to declare.

Acknowledgements

This work is supported by the National Natural Science Foundation of China (No. 22288101, 21972136, 21991090, 21991091, and 22102177).

Notes and references

1 A. M. Seayad and D. M. Antonelli, *Adv. Mater.*, 2004, **16**, 765–777.
2 C. F. Shih, T. Zhang, J. Li and C. Bai, *Joule*, 2018, **2**, 1925–1949.
3 T. He, P. Pachfule, H. Wu, Q. Xu and P. Chen, *Nat. Rev. Mater.*, 2016, **1**, 16059.
4 P. T. Aakko-Saksa, C. Cook, J. Kiviaho and T. Repo, *J. Power Sources*, 2018, **396**, 803–823.
5 T. He, Q. Pei and P. Chen, *J. Energy Chem.*, 2015, **24**, 587–594.
6 M. Nielsen, E. Alberico, W. Baumann, H. J. Drexler, H. Junge, S. Gladiali and M. Beller, *Nature*, 2013, **495**, 85–89.
7 T. H. Seiichiro Imamura, Y. Saito, H. Aritani, Y. M. Hiroyoshi Kanai and N. Tsuda, *Catal. Today*, 1999, **50**, 369–380.
8 C.-L. Li and Y.-C. Lin, *Catal. Lett.*, 2010, **140**, 69–76.
9 L. Lin, W. Zhou, R. Gao, S. Yao, X. Zhang, W. Xu, S. Zheng, Z. Jiang, Q. Yu, Y. W. Li, C. Shi, X. D. Wen and D. Ma, *Nature*, 2017, **544**, 80–83.
10 Z. Sun, X. Zhang, H. Li, T. Liu, S. Sang, S. Chen, L. Duan, L. Zeng, W. Xiang and J. Gong, *Appl. Catal., B*, 2020, **269**, 118758.
11 B. A. Peppley, J. C. Amphlett, L. M. Kearns and R. F. Mann, *Appl. Catal., A*, 1999, **179**, 21–29.
12 B. A. Peppley, J. C. Amphlett, L. M. Kearns and R. F. Mann, *Appl. Catal., A*, 1999, **179**, 31–49.
13 T. M. Nobuhiro Iwasa, N. Ogawa, K. Sakata and N. Takezawa, *Catal. Lett.*, 1998, **54**, 119–123.
14 D. Li, Y. Li, X. Liu, Y. Guo, C.-W. Pao, J.-L. Chen, Y. Hu and Y. Wang, *ACS Catal.*, 2019, **9**, 9671–9682.
15 C. S. R. Azenha, C. Mateos-Pedrero, S. Queirós, P. Concepción and A. Mendes, *Appl. Catal., B*, 2017, **203**, 400–407.
16 M. R. Kosinski, A. J. Vizcaíno, L. M. Gómez-Sainero, A. Carrero and R. T. Baker, *Appl. Catal., B*, 2021, **286**, 119935.
17 L. Arroyo-Ramírez, C. Chen, M. Cargnello, C. B. Murray, P. Fornasiero and R. J. Gorte, *J. Mater. Chem. A*, 2014, **2**, 19509–19514.
18 M. Kusche, F. Enzenberger, S. Bajus, H. Niedermeyer, A. Bosmann, A. Kaftan, M. Laurin, J. Libuda and P. Wasserscheid, *Angew. Chem., Int. Ed.*, 2013, **52**, 5028–5032.
19 L. Lin, Q. Yu, M. Peng, A. Li, S. Yao, S. Tian, X. Liu, A. Li, Z. Jiang, R. Gao, X. Han, Y. W. Li, X. D. Wen, W. Zhou and D. Ma, *J. Am. Chem. Soc.*, 2021, **143**, 309–317.
20 T. Lunkenbein, J. Schumann, M. Behrens, R. Schlogl and M. G. Willinger, *Angew. Chem., Int. Ed.*, 2015, **54**, 4544–4548.
21 F. Bossola, T. Roongcharoen, M. Coduri, C. Evangelisti, F. Somodi, L. Sementa, A. Fortunelli and V. Dal Santo, *Appl. Catal., B*, 2021, **297**, 120398.
22 H. Li, H. Tian, S. Chen, Z. Sun, T. Liu, R. Liu, S. Assabumrungrat, J. Saupsor, R. Mu, C. Pei and J. Gong, *Appl. Catal., B*, 2020, **276**, 119052.
23 J. Papavasiliou, G. Avgouropoulos and T. Ioannides, *Appl. Catal., B*, 2007, **69**, 226–234.
24 P. Ribeirinha, C. Mateos-Pedrero, M. Boaventura, J. Sousa and A. Mendes, *Appl. Catal., B*, 2018, **221**, 371–379.
25 C. Mateos-Pedrero, H. Silva, D. A. Pacheco Tanaka, S. Liguori, A. Iulianelli, A. Basile and A. Mendes, *Appl. Catal., B*, 2015, **174–175**, 67–76.
26 M. S. Spencer, *Nature*, 1986, **323**, 685–687.
27 F. Bossola, N. Scotti, F. Somodi, M. Coduri, C. Evangelisti and V. Dal Santo, *Appl. Catal., B*, 2019, **258**, 118016.
28 L. Liu, M. Lopez-Haro, C. W. Lopes, S. Rojas-Buzo, P. Concepcion, R. Manzorro, L. Simonelli, A. Sattler, P. Serna, J. J. Calvino and A. Corma, *Nat. Catal.*, 2020, **3**, 628–638.
29 Q. Sun, N. Wang, Q. Bing, R. Si, J. Liu, R. Bai, P. Zhang, M. Jia and J. Yu, *Chem*, 2017, **3**, 477–493.
30 J. Zhang, L. Wang, B. Zhang, H. Zhao, U. Kolb, Y. Zhu, L. Liu, Y. Han, G. Wang, C. Wang, D. S. Su, B. C. Gates and F.-S. Xiao, *Nat. Catal.*, 2018, **1**, 540–546.
31 Z. Yang, H. Li, H. Zhou, L. Wang, L. Wang, Q. Zhu, J. Xiao, X. Meng, J. Chen and F. S. Xiao, *J. Am. Chem. Soc.*, 2020, **142**, 16429–16436.
32 J. Zhu, R. Osuga, R. Ishikawa, N. Shibata, Y. Ikuhara, J. N. Kondo, M. Ogura, J. Yu, T. Wakihara, Z. Liu and T. Okubo, *Angew. Chem., Int. Ed.*, 2020, **59**, 19669–19674.
33 C. Wang, J. Zhang, G. Qin, L. Wang, E. Zuidema, Q. Yang, S. Dang, C. Yang, J. Xiao, X. Meng, C. Mesters and F.-S. Xiao, *Chem*, 2020, **6**, 646–657.
34 N. Wang, Q. Sun and J. Yu, *Adv. Mater.*, 2019, **31**, e1803966.
35 L. Ding, T. Shi, J. Gu, Y. Cui, Z. Zhang, C. Yang, T. Chen, M. Lin, P. Wang, N. Xue, L. Peng, X. Guo, Y. Zhu, Z. Chen and W. Ding, *Chem*, 2020, **6**, 2673–2689.
36 Q. Zhao, C. Liao, G. Chen, R. Liu, Z. Wang, A. Xu, S. Ji, K. Shih, L. Zhu and T. Duan, *Inorg. Chem.*, 2022, **61**(49), 20133–20143.
37 G. C. Chinchen, C. M. Hay, H. D. Vandervell and K. C. Waugh, *J. Catal.*, 1987, **103**, 79–86.
38 L. Lin, P. Cao, J. Pang, Z. Wang, Q. Jiang, Y. Su, R. Chen, Z. Wu, M. Zheng and W. Luo, *J. Catal.*, 2022, **413**, 565–574.
39 J. Pang, M. Zheng, C. Wang, X. Yang, H. Liu, X. Liu, J. Sun, Y. Wang and T. Zhang, *ACS Catal.*, 2020, **10**, 13624–13629.
40 D. Yu, W. Dai, G. Wu, N. Guan and L. Li, *Chin. J. Catal.*, 2019, **40**, 1375–1384.
41 Z.-Q. Wang, Z.-N. Xu, S.-Y. Peng, M.-J. Zhang, G. Lu, Q.-S. Chen, Y. Chen and G.-C. Guo, *ACS Catal.*, 2015, **5**, 4255–4259.
42 J. Gong, H. Yue, Y. Zhao, S. Zhao, L. Zhao, J. Lv, S. Wang and X. Ma, *J. Am. Chem. Soc.*, 2012, **134**, 13922–13925.
43 D. Li, F. Xu, X. Tang, S. Dai, T. Pu, X. Liu, P. Tian, F. Xuan, Z. Xu, I. E. Wachs and M. Zhu, *Nat. Catal.*, 2022, **5**, 99–108.

